

Picosecond Laser Processing of Hierarchical Micro–Nanostructures on Titanium Alloy upon Pre- and Postanodization: Morphological, Structural, and Chemical Effects

Heike Voss, Xenia Knigge, Dominik Knapic, Matthias Weise, Mario Sahre, Andreas Hertwig, Alessio Sacco, Andrea Mario Rossi, Jörg Radnik, Kai Müller, Karsten Wasmuth, Jörg Krüger, Achim Walter Hassel, Vasile-Dan Hodoroaba, and Jörn Bonse*


Recent publications indicate that the order of electrochemical anodization (before or after the laser processing step) plays an important role for the response of bone-forming osteoblasts—an effect that can be utilized for improving permanent dental or removable bone implants. For exploring these different surface functionalities, multimethod morphological, structural, and chemical characterizations are performed in combination with electrochemical pre- and postanodization for two different characteristic microspikes covered by nanometric laser-induced periodic surface structures on Ti–6Al–4V upon irradiation with near-infrared ps-laser pulses (1030 nm wavelength, ≈ 1 ps pulse duration, 67 and 80 kHz pulse repetition frequency) at two distinct sets of laser fluence and beam scanning parameters. This work involves morphological and topographical investigations by scanning electron microscopy and white light interference microscopy, structural material examinations via X-ray diffraction, and micro-Raman spectroscopy, as well as near-surface chemical analyses by X-ray photoelectron spectroscopy and hard X-ray photoelectron spectroscopy. The results allow to qualify the mean laser ablation depth, assess the spike geometry and surface roughness parameters, and provide new detailed insights into the near-surface oxidation that may affect the different cell growth behavior for pre- or postanodized medical implants.

1. Introduction

The processing of titanium by lasers offers a great potential for prosthetic medical applications because it provides a contactless, aseptic, reliable, fast, and industrially scalable approach. Here, particularly ultrashort pulsed lasers gained attention because, compared to lasers with longer pulse durations in the nanosecond range, the so-called heat-affected zone is reduced,^[1] allowing for a near-surface material functionalization without significantly affecting the mechanical properties of the work-piece/implant.^[2]

A very appealing technological approach of surface functionalization is the processing of so-called “laser-induced periodic surface structures” (LIPSS).^[3–6] These nanostructures typically form at laser fluences (areal optical energy densities in J cm^{-2}) close to the laser ablation threshold of the irradiated solids and can feature spatial periods ranging from a few micrometers down to some tens of nanometers only when ultrashort laser pulses and

H. Voss, X. Knigge, M. Weise, M. Sahre, A. Hertwig, J. Radnik, K. Müller, K. Wasmuth, J. Krüger, V. D. Hodoroaba, J. Bonse
Bundesanstalt für Materialforschung und -prüfung (BAM)
Unter den Eichen 87, 12205 Berlin, Germany
E-mail: joern.bonse@bam.de

 The ORCID identification number(s) for the author(s) of this article can be found under <https://doi.org/10.1002/pssa.202300920>.

© 2024 The Author(s). physica status solidi (a) applications and materials science published by Wiley-VCH GmbH. This is an open access article under the terms of the Creative Commons Attribution License, which permits use, distribution and reproduction in any medium, provided the original work is properly cited.

DOI: 10.1002/pssa.202300920

D. Knapic, A. W. Hassel
Institute of Chemical Technology of Inorganic Materials
Johannes Kepler University Linz
Altenberger Str. 69, 4040 Linz, Austria

A. Sacco, A. M. Rossi
Istituto Nazionale di Ricerca Metrologica (INRiM)
Strada delle Cacce 91, 10135 Torino, Italy

optimized irradiation strategies are employed for suitable materials.^[7] Such LIPSS enable a variety of surface functionalizations, including the development of bacteria-repellent surfaces^[8–10] or technical surfaces being antiadhesive for nanofibers,^[11] the reduction of friction and wear,^[12,13] and other applications.^[7,14–18] At significantly higher laser fluences, other characteristic types of laser-generated surface structures may form, such as periodic “grooves” or irregular micrometric “spikes” (sometimes called microcones).^[19–21]

It was shown already that the adhesion of scar-forming fibroblasts on titanium-based medical implant materials can be altered by a laser-processed hierarchical micro–nano surface structure.^[22,23] Such hierarchical structures can be easily generated in a single processing step in a “self-ordered” way via fs- and ps-laser-based scan processing.^[7] While the most intense central part of the Gaussian laser beam profile creates micrometric spikes in the focal region, the low intensity wing of this beam profile subsequently “overwrites” the microstructures, thus adding the LIPSS as a submicrometric surface finish.

Many medical implants are usually made from anodized Ti alloys and such a laser-based surface processing is appealing to alter the response for the osteoblasts—an effect that can be utilized for improving permanent dental or removable bone-screw implants. Recent publications indicate that the order of electrochemical anodization (before or after the laser processing step) plays an important role for the response of bone-forming osteoblasts by either enhancing or inhibiting cell growth.^[24]

To further explore these different surface functionalities, in this work two different hierarchical micro–nanospikes, named Spikes-1 and Spikes-2 in the following, were laser-processed on flat Ti–6Al–4V alloy samples with pristine polished, pre- and postanodization surface preparation. Multimethod chemical and structural characterizations were performed to determine the influence of the laser processing parameters and the order of processing on the morphology, topography, material structure, and chemical surface composition.

2. Experimental Section

2.1. Sample Preparation and Characterization

Flat titanium (Ti–6Al–4V) (Hempel Special Metals AG, Dübendorf, Switzerland) disc-shaped samples with 22 mm diameter and 2 mm thickness were mechanically ground (220, 400, 600, 1000, 2500, 4000 grit sandpaper) and polished with silica solution (50 nm particle diameter) resulting in a mirror-like surface finish (average surface roughness $R_a < 3$ nm). After surface preparation, the samples were cleaned in an ultrasonic bath with distilled water and isopropanol.

Potentiostatic preanodization was achieved by dipping only half of the sample into 3 M H_3PO_4 solution which was used as an electrolyte. The preanodization was carried out at a potential of 95 V for 100 s. This resulted in the formation of a superficial layer of turquoise color as visible in the photograph of the sample in **Figure 1b**, in accordance with the oxidation conditions found on many medical implants, in order to mimic the conditions used in ref. [24]. Subsequently, the samples were ps-laser-processed to create hierarchical micro–nanospikes.

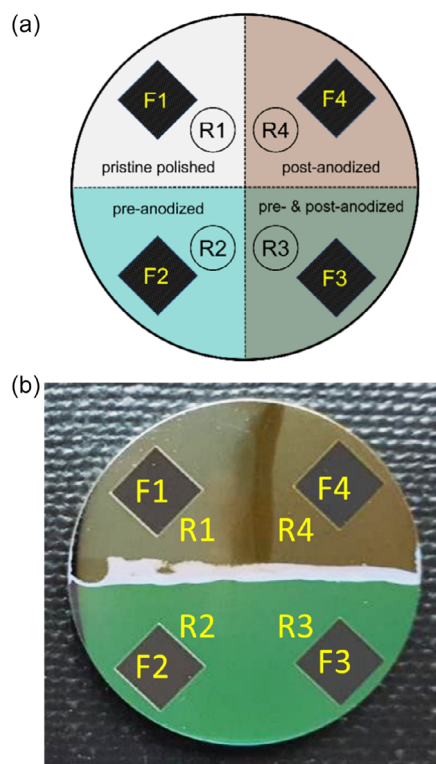


Figure 1. Layout of Ti–6Al–4V alloy samples: a) schematic drawing and b) photograph of the sample. Four 4×4 mm² laser-processed areas F1–F4 on differently anodized surfaces (R1–R4) of the polished sample: F1 on pristine polished, F2 on preanodized, F3 on pre- and postanodized, and F4 on postanodized sample surfaces.

For the postanodization step following the laser processing (for details, see Section 2.2), the samples were rotated by 90° compared to the initial preanodization step in order to realize four different combinations of pristine (only polished) and pre- and postanodization treatments. The resulting sample layout with laser-processed fields F1 to F4 on pristine polished (R1), preanodized (R2), pre- and postanodized (R3), or postanodized sample surface (R4) is shown in Figure 1a.

The potentiodynamic postanodization was performed in 0.1 M H_2SO_4 electrolyte with a scan rate of 100 mV s^{−1} and a potential up to 10 V, resulting in a brown colored oxide layer as visible on the right-hand side of the sample in Figure 1b. More details on the electrochemical anodization can be found in ref. [25].

2.2. Picosecond Laser Processing

In between pre- and postanodization steps, the samples were laser-processed with a picosecond laser in order to form self-organized hierarchical micro–nanostructures named “spikes.” The laser used is an industrial thin disc laser system TRUMPF TruMicro 5050 femto edition (Ditzingen, Germany), operated at 1030 nm wavelength with a pulse duration of 925 fs. The laser radiation was focused to a 57 μm Gaussian spot radius ($1/e^2$ -decay) with an F-Theta-lens (focal length 423 mm) and deflected with an X–Y Galvo-scanner system (ScanLab HurrySCAN II 14, Puchheim, Germany). Four areas of

$4 \times 4 \text{ mm}^2$ per sample were laser-processed in a meandering way, as visible as dark fields F1–F4 in Figure 1b. The linear polarization direction was perpendicular to the laser-processed line.

Apart from the peak fluence (F_0) that can be controlled by the laser pulse energy E_p and the Gaussian beam $1/e^2$ -radius w_0 via $F_0 = 2 \cdot E_p / (\pi \cdot w_0^2)$, another key parameter of laser processing is the “number of laser pulses per spot.” While that definition is clear for static laser processing (where the focused laser beam always hits the same spot at the sample surface), for scanning laser processing the concept of the “effective number of laser pulses” has been found to be useful.^[26] Often the 1D approach of the effective number of laser pulses per beam spot diameter is used. For processing with a Gaussian beam (diameter $2w_0$) scanned at a pulse repetition frequency f_{rep} with a constant velocity (v_x) in a line across the surface, that number accounts to N_{eff} (1D) = $(2w_0 \cdot f_{\text{rep}}) / v_x$. Extending the laser processing to 2D areas in a meandering approach with a scan line separation Δy , the 2D analogy of the effective number of laser pulses per beam spot diameter can be defined as N_{eff} (2D) = $(\pi \cdot w_0^2 \cdot f_{\text{rep}}) / (v_x \cdot \Delta y)$.

Two different sets of laser processing parameters were chosen to create distinct hierarchical micro–nanospikes named Spikes-1 and Spikes-2 on two samples each. Spikes-2 were optimized for a processing speed with a higher laser repetition rate of 80 kHz, a faster line scanning velocity of 49.5 mm s^{-1} and a larger vertical scan line separation of $40 \mu\text{m}$ at a peak fluence of 1.35 J cm^{-2} , resulting altogether in a lower spot density (number of effective pulses N_{eff} (2D) = 415) and a shorter total processing duration when compared to Spikes-1. The latter were processed with a repetition rate of 67 kHz, a line scanning velocity of 7.3 mm s^{-1} , and a line separation of $32 \mu\text{m}$ at a peak fluence of 1.16 J cm^{-2} , resulting altogether in a much higher spot density (N_{eff} (2D) = 2950). **Table 1** compiles the laser processing parameters for both types of spikes.

In order to minimize the detection limit for X-ray analyses, enlarged surface areas of $1 \times 12 \text{ mm}^2$ were processed on an additional sample (denoted with an asterisk (*) in the following) with otherwise identical laser manufacturing of Spikes-1 and Spikes-2 and electrochemical pre- and postanodization steps.

2.3. Surface Characterization

2.3.1. Scanning Electron Microscopy

Characterization of the surface morphology of the ps-laser-processed micro–nanostructures was performed with a ZEISS

Table 1. Laser irradiation parameters used for the processing of two different types of spikes. All other laser processing parameters were kept constant: beam diameter $2w_0 = 114 \mu\text{m}$, pulse duration $\tau = 925 \text{ fs}$, wavelength $\lambda = 1030 \text{ nm}$.

| Type of morphology | Spikes-1 | Spikes-2 |
|---|----------|----------|
| Peak fluence F_0 [J cm^{-2}] | 1.16 | 1.35 |
| Pulse repetition frequency f_{rep} [kHz] | 67 | 80 |
| Scanning velocity v_x [mm s^{-1}] | 7.3 | 49.5 |
| Line separation Δy [μm] | 32 | 40 |
| Number of effective pulses N_{eff} (1D) | 1050 | 185 |
| Number of effective pulses N_{eff} (2D) | 2950 | 415 |

Supra 40 (Oberkochen, Germany) scanning electron microscope (SEM), operated in InLens mode at 10 kV electron acceleration voltage. It was not necessary to coat the sample surfaces for good conductivity.

2.3.2. White Light Interference Microscopy

The surface topography was characterized with a scanning white light interference microscope (WLIM) NexView from Zygo (Middlefield, USA), allowing to acquire 3D images with a vertical (z-) resolution in the lower nm range. To quantify the difference in spike height, a statistical measurement of the surface roughness was performed with WLIM. The measurement conditions, using a $20\times$ Mirau interferometer objective with a lateral optical resolution of $0.7 \mu\text{m}$, were chosen for the surface roughness of the pristine polished sample surface with a measurement area of $420 \times 420 \mu\text{m}^2$ and an average of 14 scan lines perpendicular to the laser scanning direction. With the same algorithm, the spike areas were characterized and served as a benchmark for comparison of the average spike height.

WLIM profiles taken across the edge of laser-processed to non-processed sample areas allowed measurements of the average ablation depth due to the material removal during laser processing. Within an imaged region of $828 \times 828 \mu\text{m}^2$ centered on the edge of the laser-processed area, two regions of $\approx 800 \times 300 \mu\text{m}^2$ were defined: one region of the non-processed sample surface and another one of the laser-processed sample area, omitting the transition region. The difference in average height of these regions then indicates the average ablation depth.

2.3.3. Variable Angle Spectroscopic Ellipsometry

Thickness of the pre- and postanodization layers was measured with a goniospectral ellipsometer (model Woollam M2000DI, Lincoln, USA) with a spectral range of 192–1697 nm at incidence angles of 65° , 70° , and 75° . Given the small size of the suitable reference positions (R1–R4), a set of focusing/collimation lenses was inserted in the ellipsometer beam path for realizing a measurement spot size of $\approx 0.2 \times 0.3 \text{ mm}^2$ at 65° angle of incidence. The ellipsometric transfer quantities were determined for these measurement conditions and wavelength range, respectively. Measurement and analysis were performed using the CompleteEASE software (CEASE, Woollam, Lincoln, USA), v. 6.57 for measurement and v. 6.70 for analysis. The fit model for the analysis is a single TiO_2 layer homogeneously covering the Ti–6Al–4V sample. In a first step, the bulk dielectric properties of Ti–6Al–4V were determined at the R1 (not anodized, polished surface) position by fitting the measurement to a bulk model covered by a native oxide layer (assumed as database TiO_2 from the CEASE software data collection). With that input, the thickness values as well as the dielectric function of the covering oxide layers were then fitted for the measurements performed at all reference positions (R2 to R4). The dielectric function of the TiO_2 layer was modeled as a Kramers–Kronig-consistent spline function.

The spectroscopic ellipsometry (SE) measurement of the samples revealed a native oxide layer thickness (R1) of $\approx 8.1 \text{ nm}$, a preanodization oxide layer thicknesses around 213 nm

Table 2. Oxide layer thicknesses as evaluated via SE for pre- and postanodized oxide films on the polished Ti–6Al–4V at the four reference positions R1–R4. The uncertainty of the layer thickness is obtained from the least-squares-fits of the ellipsometric data to the single oxide layer model.

| Position | Anodization state | Oxide layer thickness [nm] |
|----------|-------------------|----------------------------|
| R1 | None (pristine) | 8.1 ± 0.8 |
| R2 | Pre- | 213.0 ± 0.4 |
| R3 | Pre- and post- | 212.6 ± 0.1 |
| R4 | Post- | 28.0 ± 0.2 |

(R2, R3), and a postanodization oxide layer thickness of ≈ 28 nm (R4). The large difference between the pre- and postanodization oxide layer thicknesses arises from the different static/dynamic electrochemical anodization modes chosen here to mimic the conditions realized in ref. [24]. **Table 2** compiles the individual oxide layer thicknesses along with the uncertainty of the least-squares-fits of the ellipsometric data evaluation to the single oxide layer model.

2.3.4. X-ray Diffraction

X-ray analysis of the laser-structured fields as well as the reference fields was performed with an X-ray diffractometer (Seifert XRD 3000 TT, Ahrensburg, Germany, Cu K α tube). Its parameters were set to 40 kV electron acceleration voltage, 40 mA current, angle steps of 0.05° and 2 s measurement time per step. The measurements were performed either in Bragg–Brentano (BB) geometry or in a grazing incidence configuration (GIXRD) with an incident angle $\Omega = 2^\circ$ using an X-ray beam collimated by a Göbel mirror. In this GIXRD geometry, the probed area was about $10 \times 12 \text{ mm}^2$. For titanium alloy, the information depths then amount to $< 10 \mu\text{m}$ (BB) and $< 0.3 \mu\text{m}$ (GIXRD), respectively.

2.3.5. Micro-Raman Spectroscopy

Confocal micro-Raman spectroscopic measurements using a DXR Raman microscope (Thermo Scientific, Waltham, USA) were performed in a 180° backscattering geometry using a frequency-doubled Nd:YAG laser operated at 532 nm wavelength. A 10 \times microscope objective (numerical aperture NA = 0.25) was employed to focus the Raman laser beam to a spot diameter (full width at half maximum) of $\approx 2.5 \mu\text{m}$ at the sample surface, while providing an average laser power of 3.0 mW. The spectral resolution of the apparatus was 5 cm^{-1} . For each sample location, the Raman spectra were averaged over $30 \times 250 \mu\text{m}^2$ maps to capture the possible spectral variance due to local inhomogeneity of the surface at the micrometer scale, sampled with $5 \mu\text{m}$ pixel lateral size and acquired for 1 s each.

2.3.6. X-ray Photoelectron Spectroscopy

To analyze the physiochemical composition of the surface, surveys and detailed spectra were taken with X-ray photoelectron spectroscopy (XPS) and hard X-ray photoelectron spectroscopy

(HAXPES) with a “Quantes” system (ULVAC-PHI, USA). The system is equipped with two X-ray sources. On the one hand, there is a monochromatic Al K α source at 1486.6 eV for XPS, which allows an insight to the sample depth of up to ≈ 10 nm. On the other hand, there is a monochromatic Cr K α source at 5414.8 eV for HAXPES, which probes information to a depth of about 30 nm below the surface. The spectrometer allows both excitations to be performed at the exact same position on the sample. As a result, the elemental composition was quantified with both, XPS and HAXPES. Moreover, from high-resolution spectra it is also possible to make statements about the surface chemistry of the probed sample location.

The size of the X-ray spot was adjusted to 100 μm . The time per step was 50 ms. Survey spectra for an overview of the elemental composition were acquired at 280 eV pass energy and an energy step size of 1 eV, while high-resolution spectra have been recorded at 55 eV pass energy and 0.1 eV energy step size for XPS and 69 eV pass energy and 0.125 eV step size for HAXPES. The beam settings were 25 W and 15 kV for XPS measurements and 50 W, 20 kV for HAXPES measurements. To get a better signal-to-noise ratio, measurements were repeated in cycles which led to a total measurement duration of about 20 h on each spot of the sample, i.e., ≈ 320 h in total for both samples. The carbon C 1s peak at 285.0 eV served as the reference signal. Experimental differences in this peak energy due to charging of the surface during the measurements were used for a correction (shift) of the binding energies of all other lines. The experimental uncertainty of the binding energy in both the XPS and HAXPES measurements was below 0.4 eV.

3. Results and Discussion

3.1. Surface Morphology and Topography

The surface morphology was analyzed on the micro- and nanometer scale by SEM (Section 3.1.1), while the surface topography was analyzed by WLM (Section 3.1.2), giving quantitative access to depth information and surface roughness parameters.

3.1.1. Morphology: SEM

The surface morphology of the two distinct spike types was analyzed with SEM images (**Figure 2**). Spikes-2 show well-separated hierarchical spikes, with pronounced nanometric low spatial frequency LIPSS (LSFL) on top of the spikes and an even height distribution. In contrast, Spikes-1 appear to be denser spaced without the deep valleys separating adjacent spikes and have an altogether uneven distribution. They are not covered by LSFL, but rather ball-shaped nano-sized features. The lack of regular LSFL on the Spikes-1 originates from the different laser processing conditions, i.e., mainly the ≈ 7 -times larger number of effective laser pulses ($N_{\text{eff}}(2\text{D}) = 2950$) compared to the Spikes-2 morphology ($N_{\text{eff}}(2\text{D}) = 415$), see Table 1. LSFL are most pronounced in specific fluence and pulse number ranges and typically become irregular and fade away for a large number of laser pulses per spot.^[27,28]

Importantly, the anodization state (none, pre-, or postanodization, pre- and postanodization) does not significantly influence the surface morphology that is ruled by the laser processing

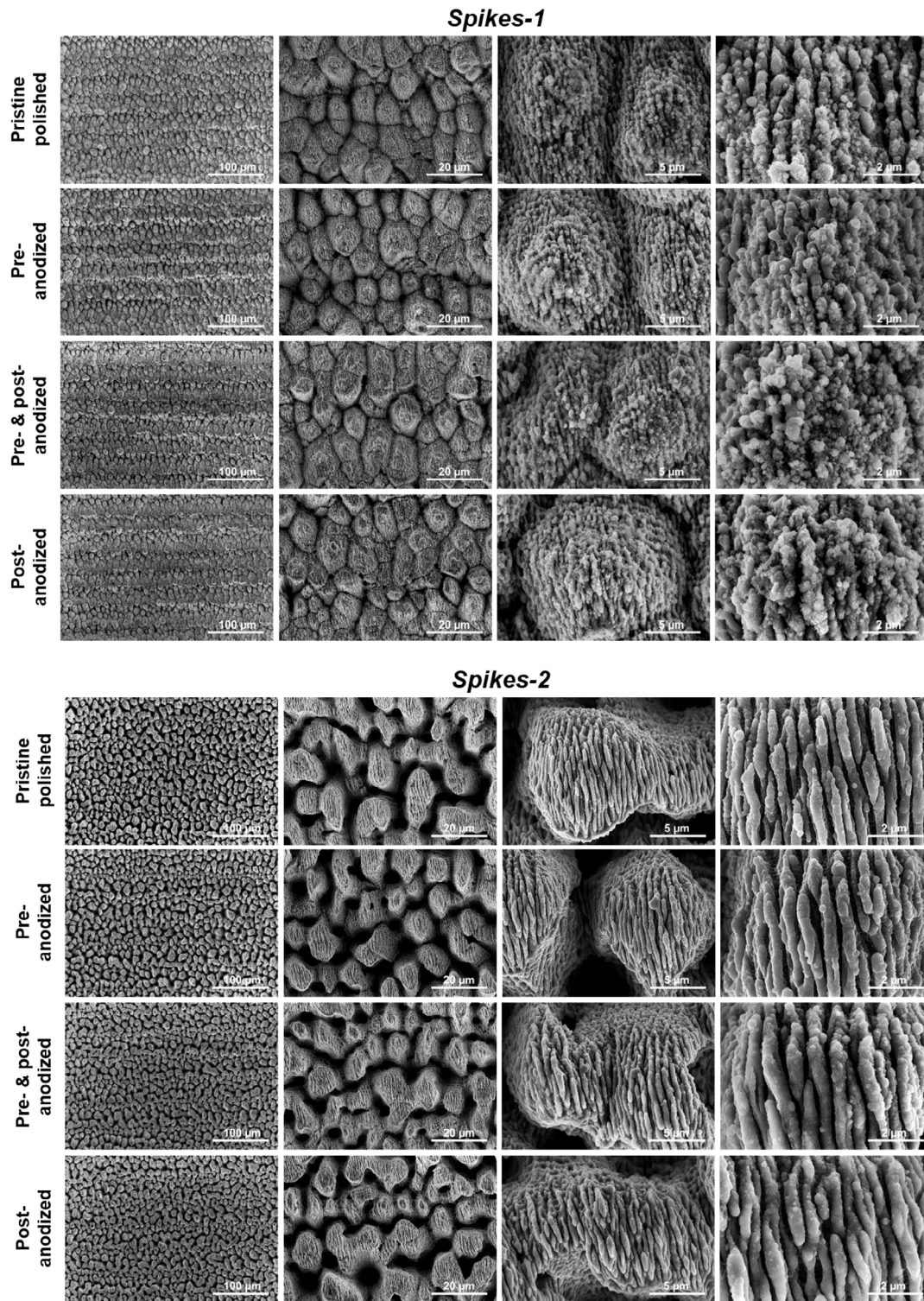


Figure 2. SEM micrographs of laser-processed spikes on pristine polished (R1), preanodized (R2), pre- and postanodized (R3), and postanodized (R4) sample surfaces for two distinct laser processing parameter sets named Spikes-1 (top panel) and Spikes-2 (bottom panel).

conditions. In other words, the presence of preanodized oxide layers of thicknesses up to ≈ 215 nm does not affect the final laser-processed surface morphologies.

The ps-laser processing parameters for Spikes-1 are adopted from the conditions for laser processing of the bone screws.^[24] Spikes-2 were optimized for production conditions of medical

implants. Comparing the Spikes-2 to the Spikes-1, the number of pulses per area is much lower, i.e., $N_{\text{eff}}(2D) = 415$ versus $N_{\text{eff}}(2D) = 2950$. This results in shorter processing duration with an eightfold increase in throughput as well as lower average ablation depths.

3.1.2. Topography: WLIM

Results of the topography measurements of ablation depth and surface roughness parameters with WLIM are listed in **Table 3** for both spike types and all anodization conditions. While the anodization of the surface does not have a big influence on the ablation depth, the type of spikes, i.e., the laser processing condition, clearly has. Spikes-2 have an average ablation depth of $\approx 6\text{--}8\ \mu\text{m}$; the tops of the spikes are about even with the non-irradiated surface plane. On the other hand, the Spikes-1 have a significantly larger average ablation depth of $\approx 57\text{--}59\ \mu\text{m}$, thus the tops of the spikes are located well below the original surface plane. Here, more Ti-6Al-4V material is ablated due to the higher number of effective pulses per beam spot area ($N_{\text{eff}}(2D) = 2950$) although the laser fluence is about 14% lower (compare Table 1).

3D topography plots taken with WLIM of just the spike-covered areas (**Figure 3**) also show very little differences in

the appearance of the spikes between pristine polished and anodized surface. The Spikes-2, however, appear homogeneously distributed and of even height ($R_z \approx 18\text{--}20\ \mu\text{m}$), while the Spikes-1 show variations in height distribution and are altogether not as high ($R_z \approx 10\text{--}12\ \mu\text{m}$).

3.2. Structural Analyses

The structural state of the laser-processed and electrochemically treated Ti-6Al-4V samples was analyzed by X-ray diffraction (XRD) techniques (Section 3.2.1) for obtaining information on crystalline phases, while the near-surface layers were probed by micro-Raman spectroscopy ($\mu\text{-RS}$) (Section 3.2.2).

3.2.1. Crystalline Phases: XRD Analyses

Grazing incidence XRD (GIXRD) enables X-ray information depths in the submicrometer range and, thus, results in a high surface sensitivity. This method is particularly suitable for the flat polished, pre- or postanodized reference areas being not disturbed by large surface topographic alterations (such as the spikes). **Figure 4a** presents GIXRD data of three non-irradiated reference areas, i.e., for the pristine polished surface covered

Table 3. Mean ablation depth and spike height (maximum surface roughness R_z) and average surface roughness R_a measured by WLIM for the two spike types on the four anodization states of the sample surface (pristine, preanodized, postanodized, pre- and postanodized).

| Field | Spike type | Anodization state | Mean ablation depth [μm] | Spike height R_z [μm] | Average surface roughness R_a [μm] |
|-------|------------|-------------------|---------------------------------------|--------------------------------------|---|
| F1 | Spikes-1 | None (pristine) | 57.3 | 11.1 ± 0.9 | 2.3 ± 0.2 |
| F2 | Spikes-1 | Pre- | 59.2 | 11.7 ± 1.1 | 2.5 ± 0.3 |
| F3 | Spikes-1 | Pre- and post- | 58.1 | 11.7 ± 0.8 | 2.4 ± 0.2 |
| F4 | Spikes-1 | Post- | 58.7 | 10.1 ± 0.7 | 2.1 ± 0.1 |
| F1 | Spikes-2 | None (pristine) | 7.1 | 19.3 ± 0.7 | 4.2 ± 0.2 |
| F2 | Spikes-2 | Pre- | 7.3 | 20.1 ± 1.3 | 4.4 ± 0.3 |
| F3 | Spikes-2 | Pre- and post- | 6.5 | 18.1 ± 1.3 | 4.0 ± 0.3 |
| F4 | Spikes-2 | Post- | 6.4 | 18.4 ± 1.9 | 3.9 ± 0.4 |

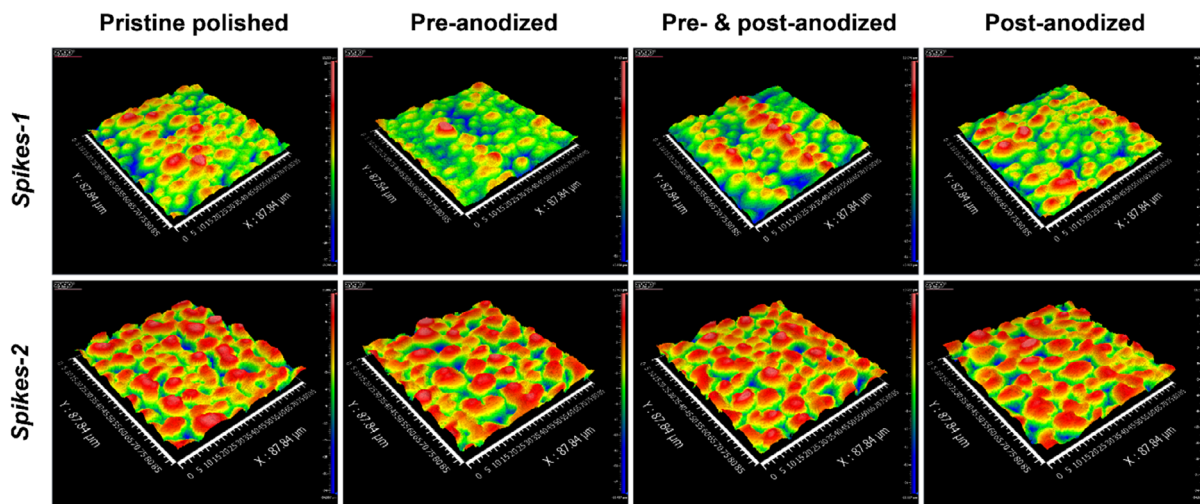


Figure 3. WLIM 3D topography images of Spikes-1 and Spikes-2.

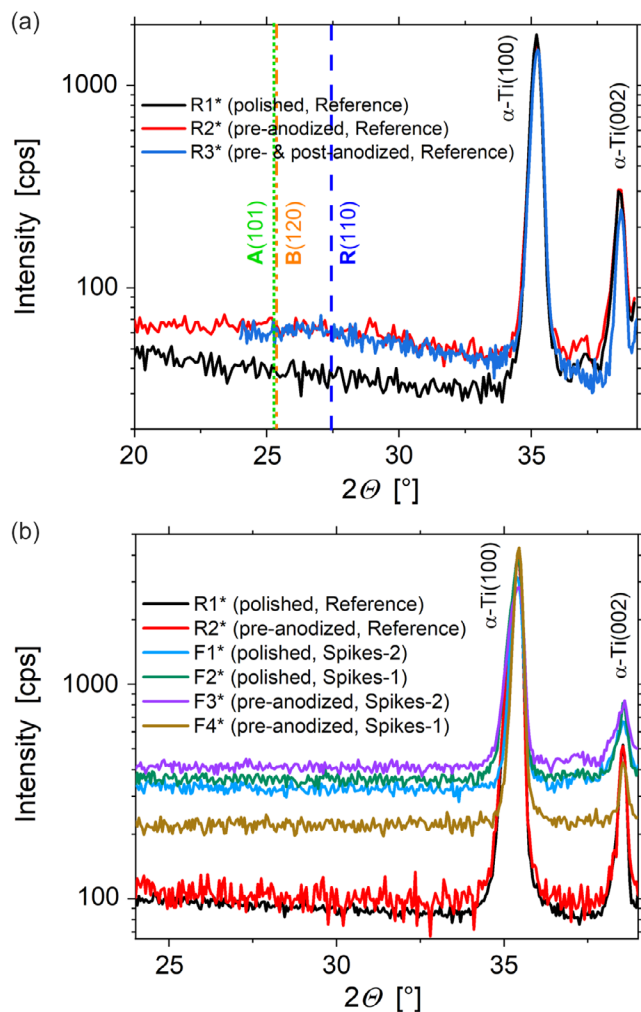


Figure 4. a) XRD grazing incidence analyses of pristine polished (R1*), preanodized (R2*), and pre- and postanodized (R3*) nonirradiated reference surface areas. The three vertical lines indicate the positions of the strongest reflexes of TiO_2 phases in the form of crystalline rutile (R, dashed line), anatase (A, dotted line), and brookite (B, dash-dotted line), as listed in the ICDD database. b) Bragg-Brentano XRD analyses of laser-processed (F2* and F4*: Spikes-1; F1* and F3*: Spikes-2) and reference areas (R1*, R2*). For better comparison, the ordinates are scaled logarithmically.

with a native oxide layer (R1*, black curve), for the preanodized polished surface (R2*, red curve), and for the pre- and postanodized polished sample surface (R3*, blue curve). All three curves are dominated by two strong diffraction signals that can be assigned to $\alpha\text{-Ti}$ (100) ($2\theta = 35.4^\circ$) and $\alpha\text{-Ti}$ (002) ($2\theta = 38.1^\circ$) Bragg reflections. Those two reflexes originate from the polycrystalline Ti-6Al-4V bulk material. Additionally, a shallow, very broad reflex centered around $2\theta = 27^\circ$ can be detected for the preanodized and the pre- and postanodized reference surface only (red and blue curves). This points toward the presence of amorphous or nanocrystalline titanium oxides with a crystallite size much smaller than the layer thickness which was measured to be ≈ 213 nm here by SE (see Table 2). In contrast, the polished reference surface covered by a native oxide just shows a weakly varying background signal in the corresponding angular range (black curve).

Measurement of the laser-processed regions was performed in focused mode BB geometry to prevent shadowing effects of the rough spike surfaces (Spikes-1 and Spikes-2). Figure 4b depicts the diffracted X-ray beam intensity in dependence of the incidence angle θ for the region between $2\theta = 20^\circ$ and 39° , where a signal of crystalline oxide phases would be expected. Again, the above mentioned reflexes of the polycrystalline Ti-6Al-4V alloy also dominate the BB-XRD spectra. Crystalline oxide phases were not detected in any of the measurements for laser-processed or reference areas.

3.2.2. Structural State: $\mu\text{-RS}$

For suitable materials, $\mu\text{-RS}$ may allow a characterization of the structural state by analyzing peaks caused by the optical excitation of material-specific phonon modes. While the Raman cross sections of bulk metals are generally very small, the method can be suitable to assess the presence of metal oxide layers.

Figure 5 compares background-corrected Raman spectra recorded under identical conditions at the laser-processed spikes (Spikes-1: F2* and F4*; Spikes-2: F1* and F3*) generated in the polished (F1* and F2*) or preanodized (F3* and F4*) sample regions. Additionally, two reference spectra from the non-irradiated regions (polished (R1*) versus preanodized (R2*)) are displayed. The top panel (a) of the figure provides an overview, while the spectra shown in the bottom panel (b) are limited to the wavenumber range below 700 cm^{-1} . Here, additionally the positions of Raman peaks of titanium dioxide (TiO_2) in its crystalline phases of rutile (R) and anatase (A), as taken from the literature, are marked via vertical dashed and dotted lines, respectively.

All Raman spectra are widely featureless and do not exhibit pronounced peaks. As expected, the signal level of both reference spectra lies below that recorded in the laser-processed regions. The increase in baselines in the lower Raman shift region in the reference spectra is caused by the difference in reflectance in the regions. The spectra taken in the laser-processed areas are quite similar in shape, featuring a very broad band around $\approx 250\text{ cm}^{-1}$, although the maximum signal level is clearly different for the two types of spikes (Spikes-1 vs Spikes-2). All the spectra (F1* to F4*) indicate the presence of amorphous oxides only, without any indications of crystalline oxide phases^[29,30]—in agreement with the XRD results. The higher Raman signal levels for the Spikes-1 morphology are consistent with a larger amount of oxidic material formed at the surface compared to the Spikes-2. This appears reasonable here because a larger N_{eff} ($1D/2D$) was used for their laser processing. As before, no significant influence of the presence of an additional preanodized oxide layer on the laser-processed spikes morphologies could be detected.

The results obtained at the LSFL-covered spike surface areas on these samples are in line with our previous $\mu\text{-RS}$ analyses on fs-laser-irradiated titanium,^[29,30] where the presence of amorphous oxides was proven for LSFL-covered titanium materials.

In summary of the structural analyses, neither XRD nor $\mu\text{-RS}$ could detect the presence of crystalline oxide phases. It must be concluded that both the anodic oxide layers and also the laser-induced oxide layers have an amorphous material structure. The native oxide layer being present on the Ti-6Al-4V alloy is too thin to be detected by these methods under the given conditions.

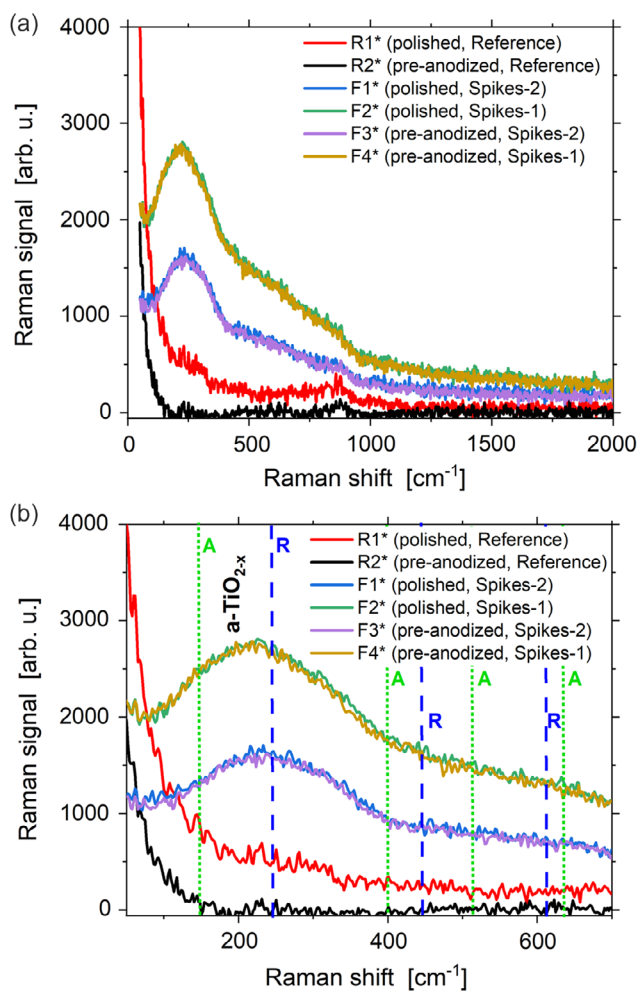


Figure 5. Raman spectra recorded in 180° backscattering geometry (532 nm) at two different ps-laser-processed spikes morphologies (Spikes-1 vs Spikes-2), generated either on a polished or a preanodized flat Ti-6Al-4V sample: a) overview and b) detail. The vertical blue and green lines in b) indicate the positions of the most intense Raman peaks of the crystalline rutile (R, dashed line) or anatase (A, dotted line) titania phases, as taken from the literature.

3.3. Surface Chemistry

The chemical state of the laser-processed and electrochemically treated Ti-6Al-4V samples was analyzed by photoelectron spectroscopy techniques (XPS and HAXPES, Section 3.3.1), probing the near-surface chemistry of the sample interface over depths ranging from a few nanometers (for XPS) up to some tens of nanometers (for HAXPES).

3.3.1. Sample Interface: XPS and HAXPES

The spectral analyses via XPS and HAXPES methods allow a quantification of the elemental composition of the sample surface. **Figure 6** compiles survey spectra recorded for Spikes-1 (a) and Spikes 2 (b), each at eight characteristic laser-processed (F1-F4) and reference (R1-R4) positions, according to the

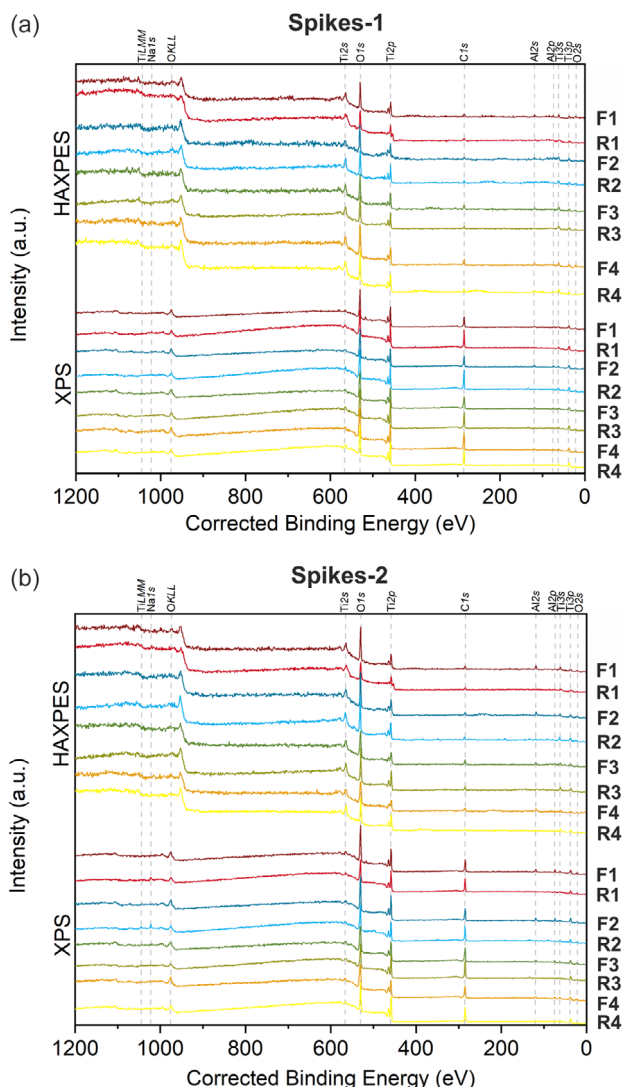


Figure 6. XPS and HAXPES survey spectra taken at different locations (references R1-R4, ps-laser-processed F1-F4) for a) Spikes-1 and b) Spikes 2.

scheme presented previously in Figure 1. The top part of the figures presents the group of HAXPES spectra, while the bottom part displays the corresponding XPS spectra.

In all survey spectra, the elements Ti, O, Al, and C as well as small amounts of Na are found to be present at the surface. Relevant signals of V were not detected here. This is consistent with the findings of Florian et al.,^[31] where a decrease of the near-surface V concentration has been detected for fs-laser-processed spikes. The direct comparison of XPS representing ≈ 10 nm information depth and HAXPES representing ≈ 30 nm information depth shows a decrease of the amount of C, as C is located on the surface of the sample in adsorbed hydrocarbon molecules from the air, so-called adventitious carbon. With both, XPS and HAXPES, a quantification of the surface composition was performed for both types of spikes.

Table 4 compiles the elemental surface composition (at %) as obtained from the corresponding XPS and HAXPES survey

Table 4. Elemental surface compositions of four ps-laser-processed Ti–6Al–4V surface areas covered with Spikes-1 (F1–F4) and the corresponding four differently anodized reference areas (R1–R4), as quantified by XPS and HAXPES with a relative uncertainty of $\approx 20\%$.

| Sample area | | F1 | R1 | F2 | R2 | F3 | R3 | F4 | R4 |
|-------------------------|-------|--------|------|------|------|------|------|------|------|
| Elemental concentration | | [At %] | | | | | | | |
| XPS | C 1s | 40.5 | 40.4 | 40.4 | 47.9 | 39.0 | 44.2 | 44.3 | 43.3 |
| | O 1s | 43.6 | 45.7 | 42.9 | 39.4 | 43.3 | 41.2 | 41.4 | 41.6 |
| | Ti 2p | 12.5 | 11.2 | 11.6 | 10.0 | 12.2 | 12.5 | 11.2 | 12.9 |
| | Al 2p | 3.4 | 2.7 | 5.1 | 2.7 | 5.5 | 2.2 | 3.0 | 2.1 |
| HAXPES | C 1s | 18.3 | 17.1 | 16.5 | 16.1 | 24.3 | 16.3 | 28.8 | 16.3 |
| | O 1s | 55.5 | 53.5 | 54.0 | 52.8 | 52.6 | 55.3 | 47.6 | 54.5 |
| | Ti 2p | 24.2 | 27.8 | 23.2 | 28.8 | 16.6 | 25.9 | 19.1 | 27.5 |
| | Al 1s | 2.0 | 1.6 | 6.4 | 2.2 | 6.4 | 2.5 | 4.6 | 1.7 |

Table 5. Elemental surface compositions of four ps-laser-processed Ti–6Al–4V surface areas covered with Spikes-2 (F1–F4) and the corresponding four differently anodized reference areas (R1–R4), as quantified by XPS and HAXPES with a relative uncertainty of $\approx 20\%$.

| Sample area | | F1 | R1 | F2 | R2 | F3 | R3 | F4 | R4 |
|-------------------------|-------|--------|------|------|------|------|------|------|------|
| Elemental concentration | | [At %] | | | | | | | |
| XPS | C 1s | 34.4 | 44.3 | 35.4 | 46.3 | 42.0 | 50.1 | 41.5 | 43.1 |
| | O 1s | 46.5 | 41.6 | 45.9 | 41.7 | 42.5 | 38.0 | 43.2 | 39.7 |
| | Ti 2p | 10.9 | 10.9 | 11.1 | 19.1 | 10.2 | 10.9 | 10.2 | 14.0 |
| | Al 2p | 8.2 | 3.1 | 7.7 | 1.9 | 5.4 | 1.0 | 5.1 | 3.2 |
| HAXPES | C 1s | 14.4 | 17.9 | 13.8 | 17.1 | 18.8 | 17.0 | 22.4 | 15.9 |
| | O 1s | 57.8 | 49.5 | 57.4 | 58.8 | 57.1 | 55.5 | 50.6 | 55.8 |
| | Ti 2p | 17.8 | 30.8 | 18.5 | 23.0 | 16.3 | 25.7 | 19.8 | 26.0 |
| | Al 1s | 10.0 | 1.8 | 10.3 | 1.1 | 7.8 | 1.8 | 7.2 | 2.3 |

spectra for the four different surface areas covered with Spikes-1 (F1–F4) and for the four differently anodized references (R1–R4), while **Table 5** provides analogous information for the sample processed with Spikes-2.

To evaluate the surface chemistry in more detail, high-resolution spectra were recorded. Measurements of Ti and Al are shown in the **Figure 7** for Spikes-2. Here, the intensity of the HAXPES signals was adjusted to be comparable to that of the XPS measurements. Due to the low kinetic photoelectron energy of ≈ 500 eV (as difference between the X-ray photon energy and binding energy), the measurement of the Ti 1s signal (**Figure 7a**) is even more surface sensitive than the Ti 2p signal in the XPS measurement (**Figure 7b**) with a kinetic energy of ≈ 1000 eV. Here, no significant differences between the various measured locations are found. The other HAXPES spectra for the Al 1s, Ti 2p, and Al 2p transitions with kinetic energies of the photoelectrons exceeding 3900 eV show differences for the reference R1 peaks at 1558 eV (for Al 1s), at 453 eV (for Ti 2p), and at 71 eV (for Al 2p), which indicates that metallic Ti and metallic Al are present underneath the surface. For some measurements at pre- or postanodized samples

(R4, R3), there is a minor shift of up to -0.5 eV observed for the 1s and 2p Ti and Al peaks present in both HAXPES and XPS modes. This shift value is close to the measurement uncertainty of 0.4 eV, but could also arise from slight chemical modifications.

The presence of metallic Ti underneath the surface is most obvious for the HAXPES spectrum of the R1 curve (red line) of the Ti 2p doublet in **Figure 7b**. Here, an additional peak can be seen at ≈ 453 eV, which can be associated with the presence of metallic Ti (Ti⁰ oxidation state). The strongest peak at ≈ 459 eV is caused by titanium in the Ti⁴⁺ oxidation state being indicative of TiO₂. Note that the peak of metallic Ti at R1 is very weak in the corresponding XPS spectrum, which originates from the different information depths of the XPS and HAXPES methods.

This finding can be explained as follows: the surface at position R1 represents the Ti–6Al–4V alloy that is covered by a native oxide layer consisting mainly of titania. According to the SE measurements, its thickness is ≈ 8 nm (see Section 2.3.3). As HAXPES exhibits an information depth of ≈ 30 nm, it can probe the bulk of the Ti alloy underneath the native oxide layer, resulting in the peak of metallic Ti at ≈ 453 eV. In contrast, the information depth of XPS is limited to ≈ 10 nm only, i.e., about the same as the thickness of the native oxide layer, resulting in a much weaker signal of the metallic titanium. For all other measurements, the surface is covered mainly by TiO₂, regardless, whether it was processed by pre- or postanodization or by an additional laser treatment. The thicknesses of these electrochemically anodized or laser-induced layers are always larger than the XPS and HAXPES maximum information depths of ≈ 10 and 30 nm, respectively. For the pre- and postanodized polished sample surfaces (R2–R4), this is again consistent with the SE measurements that revealed titania film thicknesses of ≈ 213 or 28 nm. For the laser-processed spikes structures (F1–F4), the results are also consistent with the little available literature that indicates an overall increase of thickness of the oxide layer on spikes generated by ultrashort pulse laser processing in air environment.^[31,32] The small shifts of the Ti/Al peaks by up to 0.5 eV hints to slight changes in the chemical surrounding of these elements.

The spectra recorded for Spikes-1 are generally very similar to that of Spikes-2 and are not shown here for brevity. Thus, no significant differences were detected among the different laser processing conditions. Moreover, the results presented here for the XPS and HAXPES analyses of the ps-laser-generated spikes morphology are generally very similar to the ones recently reported for ps-laser-generated high spatial frequency LIPSS, so-called HSFL (type II) on Ti–6Al–4V alloy.^[33] Such nanostructures are formed slightly above the lowest threshold fluence of permanent material modification and represent a grating-like surface topography with sub-100 nm spatial periods and modulation depths of some tens of nanometers only. Given this similarity in the XPS and HAXPES results between the ps-laser-generated HSFL and spikes, it must be concluded that the ps-laser treatment of the Ti alloy in air environment at fluences exceeding the modification threshold of the material is accompanied by surface oxidation toward the formation of amorphous TiO₂ layers at the sample interface.

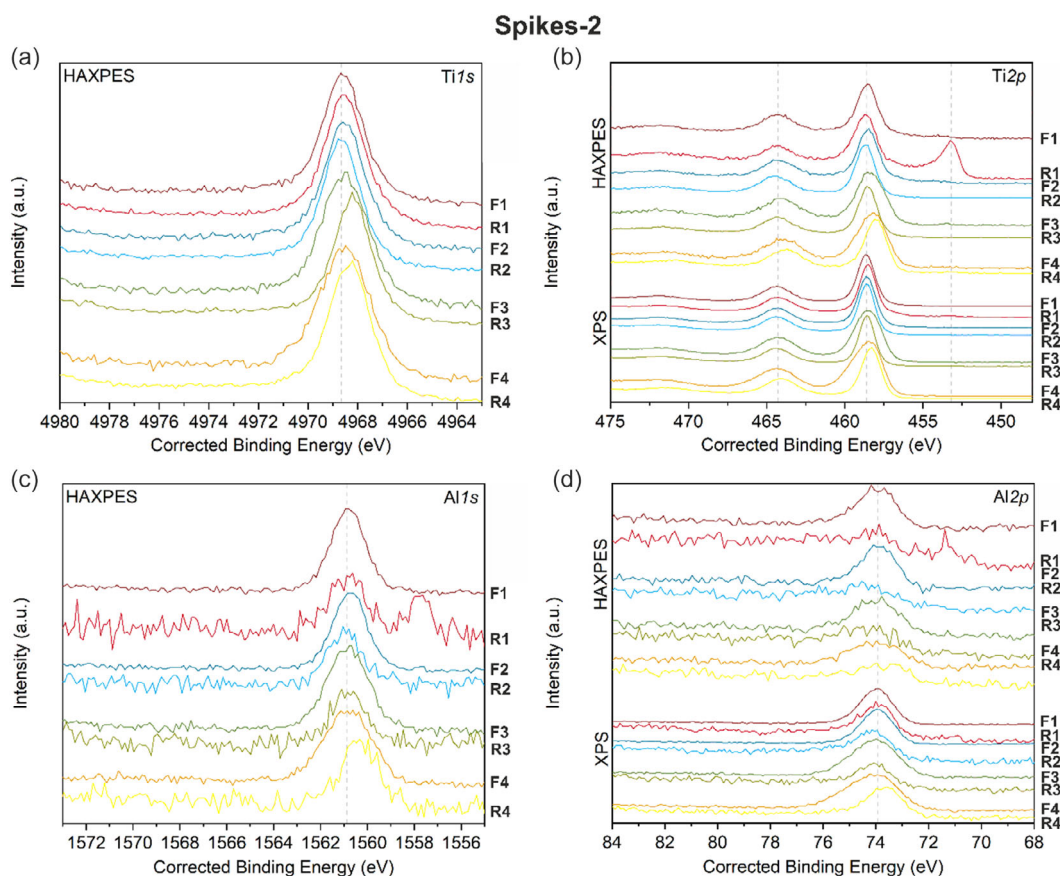


Figure 7. High-resolution XPS and HAXPES spectra taken for the a) Ti 1s, b) Ti 2p, c) Al 1s, and d) Al 2p transitions at different locations (references R1–R4, ps-laser-processed F1–F4) for a sample with Spikes-2.

3.4. Response to Osteoblast Cells

In view that we successfully reproduced by ps-laser processing the (Spikes-1) surface micro–nanostructure and electrochemical anodization conditions used in ref. [24] but that we could not detect any significant difference in the final surface chemistry with respect to additional pre- or postanodization steps, we speculate here that the different growth behavior of osteoblast cells in the Spikes-1 morphology reported in ref. [24] may result from subsurface stimuli, e.g., potentially detrimental metal ions released from the laser-processed defective subsurface regions via cracks or nanopores^[31] in the outermost defective laser-generated oxide layer. The driving force for the growth of laser-generated oxide is the diffusion of ions along the chemical gradient. Anodic oxides on the other hand are growing through a thermally activated field-assisted process that is described by the high-field mechanism. The anodization always aims at the lowest activation energy. In this way, the defects are systematically “healed” upon postanodization,^[25] thus indirectly supporting the growth of osteoblasts in combination with other surface topographic effects.

Our chemical and structural analyses indicate no significant differences among the two types of surfaces of Spikes-1 and Spikes-2, with different morphologies, as probed with XRD, μ -RS, XPS, and HAXPES. However, the specificity of these

methods is not suitable to reveal or quantify the presence of subsurface defects, such as cracks and nanopores in the subsurface laser-induced oxide layer that is covering the two different spikes’ hierarchical micro–nano topographies. Additional research on the role of subsurface defects in the laser-induced oxide layer, with respect to the response of osteoblasts cells, would be required but is beyond the scope of this work.

4. Conclusions

Morphological, structural, and chemical effects were studied for picosecond laser processing of hierarchical micro–nanostructures on Ti–6Al–4V alloy upon pre- and postanodization steps mimicking the surface functionalization of medical implants. Laser processing parameters were optimized for processing speed. SEM and WLIM allowed to characterize the multiscale surface morphology and surface roughness parameters, proving that neither an electrochemical pre- nor a postprocessing step significantly affects the geometrical surface characteristics. Structural analyses by XRD and μ -RS revealed the amorphous structural states of both the laser-modified surface layer and the anodized oxide layers. Chemical analyses of the interfacial chemistry by XPS and HAXPES indicate a ps-laser-induced oxidation process with TiO₂ being the dominant surface oxide.

Acknowledgements

This work has received funding from the European Union's Horizon 2020 research and innovation program under grant agreement no. 951730 (LaserImplant). The authors would like to thank S. Benemann (BAM 6.1) for SEM characterization.

Open access funding enabled and organized by Projekt DEAL.

Conflict of Interest

The authors declare no conflict of interest.

Data Availability Statement

The data that support the findings of this study are available from the corresponding author upon reasonable request.

Keywords

hierarchical micro–nanostructures, laser-induced periodic surface structures, Ti–6Al–4V alloys, ultrashort laser processing, X-ray photoelectron spectroscopy

Received: December 4, 2023

Revised: May 7, 2024

Published online:

- [1] D. Bäuerle, in *Laser Processing and Chemistry*, 4th ed., Springer, Berlin **2011**.
- [2] C. Symietz, E. Lehmann, R. Gildenhaar, J. Krüger, G. Berger, *Acta Biomater.* **2010**, *6*, 3318.
- [3] H. M. van Driel, J. E. Sipe, J. F. Young, *Phys. Rev. Lett.* **1982**, *49*, 1955.
- [4] J. Bonse, S. Höhm, S. V. Kirner, A. Rosenfeld, J. Krüger, *IEEE J. Sel. Top. Quantum Electron.* **2017**, *23*, 9000615.
- [5] A. Y. Vorobyev, C. Guo, *Laser Photonics Rev.* **2013**, *7*, 385.
- [6] J. Reif, in *Advances in the Application of Lasers in Materials Science* (Ed: P. Ossi), Springer, Cham, Switzerland **2018**, pp. 63–88.
- [7] J. Bonse, S. V. Kirner, J. Krüger, in *Handbook of Laser Micro- and Nano-Engineering* (Ed: K. Sugioka), Springer Nature, Cham, Switzerland **2021**, pp. 879–936.
- [8] A. M. Richter, G. Buchberger, D. Stifter, J. Duchoslav, A. Hertwig, J. Bonse, J. Heitz, K. Schwibbert, *Nanomaterials* **2021**, *11*, 3000.
- [9] K. Schwibbert, A. M. Richter, J. Krüger, J. Bonse, *Laser Photonics Rev.* **2024**, *18*, 2300753.
- [10] A. Cunha, A.-M. Elie, L. Plawinski, A. P. Serro, A. M. B. do Rego, A. Almeida, M. C. Urdaci, M.-C. Durrieu, R. Vilar, *Appl. Surf. Sci.* **2016**, *360*, 485.
- [11] S. Lifka, K. Harsányi, E. Baumgartner, L. Pichler, D. Baiko, K. Wasmuth, J. Heitz, M. Meyer, A.-C. Joel, J. Bonse, W. Baumgartner, *Beilstein J. Nanotechnol.* **2022**, *13*, 1268.
- [12] J. J. Ayerdi, N. Slachciak, I. Llavori, A. Zabala, A. Aginagalde, J. Bonse, D. Spaltmann, *Lubricants* **2019**, *7*, 79.
- [13] S. Rung, K. Bokan, F. Kleinwort, S. Schwarz, P. Simon, J.-H. Klein-Wiele, C. Esen, R. Hellmann, *Lubricants* **2019**, *7*, 43.
- [14] S. Gräf, *Adv. Opt. Technol.* **2020**, *9*, 11.
- [15] C. Florian, S. V. Kirner, J. Krüger, J. Bonse, *J. Laser Appl.* **2020**, *32*, 022063.
- [16] E. Stratakis, J. Bonse, J. Heitz, J. Siegel, G. D. Tsibidis, E. Skoulas, A. Papadopoulos, A. Mimidis, A. C. Joel, P. Comanns, J. Krüger, C. Florian, Y. Fuentes-Edfuf, J. Solis, W. Baumgartner, *Mater. Sci. Eng. R* **2020**, *141*, 100562.
- [17] M. Mezera, C. Florian, G.-W. Römer, J. Krüger, J. Bonse, in *Ultrafast Laser Nanostructuring – The Pursuit of Extreme Scales* (Eds: R. Stoian, J. Bonse), Springer Nature, Cham, Switzerland **2023**, pp. 827–886.
- [18] G. Buchberger, M. Muck, C. Plamadela, J. Heitz, in *Ultrafast Laser Nanostructuring – The Pursuit of Extreme Scales* (Eds: R. Stoian, J. Bonse), Springer Nature, Cham, Switzerland **2023**, pp. 1105–1165.
- [19] K. M. T. Ahmmed, C. Grambow, A.-M. Kietzig, *Micromachines* **2014**, *5*, 1219.
- [20] S. He, J. J. Nivas, A. Vecchione, M. Hu, S. Amoroso, *Opt. Express* **2016**, *24*, 3238.
- [21] C. A. Zuhlke, T. P. Anderson, D. R. Alexander, *Opt. Express* **2013**, *21*, 8460.
- [22] J. Heitz, C. Plamadela, M. Muck, O. Armbruster, W. Baumgartner, A. Weth, C. Steinwender, H. Blessberger, J. Kellermaier, S. V. Kirner, J. Krüger, J. Bonse, A. S. Guntner, A. W. Hassel, *Appl. Phys. A* **2017**, *123*, 734.
- [23] S. A. Lone, M. Muck, P. Fosodeder, C. C. Mardare, C. Florian, A. Weth, J. Krüger, C. Steinwender, W. Baumgartner, J. Bonse, J. Heitz, A. W. Hassel, *Phys. Status Solidi A* **2020**, *217*, 1900838.
- [24] M. Muck, B. Wolfsjäger, K. Seibert, C. Maier, S. A. Lone, A. W. Hassel, W. Baumgartner, J. Heitz, *Nanomaterials* **2021**, *11*, 1342.
- [25] D. Knapic, A. I. Mardare, H. Voss, J. Bonse, A. W. Hassel, *Phys. Status Solidi A* **2024**, *221*, 2300609.
- [26] J. Bonse, S. Gräf, *Laser Photonics Rev.* **2020**, *14*, 2000215.
- [27] J. Bonse, M. Munz, H. Sturm, *J. Appl. Phys.* **2005**, *97*, 013538.
- [28] J. Bonse, J. Krüger, *J. Appl. Phys.* **2010**, *108*, 034903.
- [29] S. V. Kirner, T. Wirth, H. Sturm, J. Krüger, J. Bonse, *J. Appl. Phys.* **2017**, *122*, 104901.
- [30] S. V. Kirner, N. Slachciak, A. Elert, M. Griepentrog, D. Fischer, A. Hertwig, M. Sahre, I. Dörfel, H. Sturm, S. Pentzien, R. Koter, D. Spaltmann, J. Krüger, J. Bonse, *Appl. Phys. A* **2018**, *124*, 326.
- [31] C. Florian, R. Wonneberger, A. Undisz, S. V. Kirner, K. Wasmuth, D. Spaltmann, J. Krüger, J. Bonse, *Appl. Phys. A* **2020**, *126*, 266.
- [32] E. Peng, R. Bell, C. A. Zuhlke, M. Wang, D. R. Alexander, G. Gogos, J. E. Shield, *J. Appl. Phys.* **2017**, *122*, 133108.
- [33] K. Müller, F. Mirabella, X. Knigge, M. Mezera, M. Weise, M. Sahre, K. Wasmuth, H. Voss, A. Hertwig, J. Krüger, J. Radnik, V.-D. Hodoroaba, J. Bonse, *Phys. Status Solidi A* **2024**, *221*, 2300719.